PCCP

ROYAL SOCIETY OF CHEMISTRY

PAPER

View Article Online
View Journal | View Issue

Check for updates

Cite this: *Phys. Chem. Chem. Phys.*, 2017, **19**, 29429

Ni supported $CdIn_2S_4$ spongy-like spheres: a noble metal free high-performance sunlight driven photocatalyst for hydrogen production†

Manh-Hiep Vu, Chinh-Chien Nguyen, M. Sakar and Trong-On Do *

Nickel supported $CdIn_2S_4$ (Ni-CIS) spongy-like spheres have been developed using alcoholysis followed by a sulfidation process. The formation of nanocrystalline-single phase $CdIn_2S_4$ was confirmed using X-ray diffraction studies. Electron microscopy images showed that the spongy-like spheres are composed of $CdIn_2S_4$ nanoparticles with average sizes of around 25 nm. X-ray photoelectron spectra indicated the presence of elements with their respective stable oxidation states that led to the formation of single phase $CdIn_2S_4$ with enhanced structural integrity and chemical composition. The absorption spectra indicated the visible light activity of the material and the band gap energy is deduced to be 2.23 eV. The photocatalytic efficiency of the synthesized Ni-CIS in relation to its ability to produce hydrogen under solar light irradiation is estimated to be 1060 μmol g^{-1} h^{-1}, which is around 5.5 and 3.6 fold higher than that of Pt-CIS (180 μmol g^{-1} h^{-1}) and Pd-CIS (290 μmol g^{-1} h^{-1}), respectively, as obtained in this study. Accordingly, the mechanism of the observed efficiency of the Ni-CIS nanoparticles is also proposed. The recyclability test showed consistent hydrogen evolution efficiency over 3 cycles (9 h), which essentially revealed the excellent photo- and chemical-stability of the photocatalyst. The strategy to utilize non-noble metals such as Ni, rather than noble-metals, as a co-catalyst opens up a new possibility to develop low cost and high-performance sunlight-driven photocatalysts as achieved in this study.

Received 6th September 2017,
Accepted 15th October 2017

DOI: 10.1039/c7cp06085h

rsc.li/pccp

1. Introduction

Photocatalytic hydrogen production using semiconductor-based photocatalysts has received significant attention as it greatly helps in solving the issues related to energy and environmental demands. Recently, metal sulfides have been considered as promising photocatalysts due to their suitable band gap energy and excellent photocatalytic activity and stability.[1–3] As compared to metal oxide based photocatalysts, sulfides are more promising as their band gap energy and band edge position can be easily tunable. It is known that in oxides, the valence band (VB) that is composed of oxygen species often suffers due to defects and other limitations such as poor band dispersion and restrained band potentials. Alternatively, the VB potential that is constructed using sulfide species offers dispersed potentials that manifest tunable band gap energies and band edge positions in semiconductors.[1,4] Among the various types of metal sulfide photocatalysts, $CdIn_2S_4$ is reported as a potential material for applications in photocatalysis and solar cells.[5,6] It is reported that the combined functional characteristics of indium and cadmium can enhance their optical and chemical properties by many folds as compared to their individual counterparts. Owing to the enhanced chemical stability and narrow band gap energy (2.2–2.4 eV), $CdIn_2S_4$ could overcome the limitation of its parent materials such as In_2S_3 and CdS.[3] However, $CdIn_2S_4$ mainly suffers due to the fast recombination of generated electron–hole pairs that eventually reduces its photocatalytic activity. It should be noted that the fast recombination of the charge carriers could be regulated *via* controlling the chemical composition (*e.g.* anion/cation defect free) of a photocatalyst and this could be effectively achieved through the synthesis processes.[7,8] Accordingly, here we have meticulously developed a $CdIn_2S_4$ phase in a two-step alcoholysis and sulfidation process at higher temperature. In addition to this, it is also realized that the coupling of $CdIn_2S_4$ with a co-catalyst can significantly improve the separation of photo-induced charge carriers and greatly reduce the recombination possibilities in $CdIn_2S_4$. Recently, nickel (Ni) has been demonstrated as an effective co-catalyst, especially for metal sulfide photocatalysts such as CdS.[9,10] Hence, the utilization of nickel-based compounds as co-catalysts to build sulfide-based

---

Department of Chemical Engineering, Laval University, Québec, G1V 0A6, Canada. E-mail: trong-on.do@gch.ulaval.ca

† Electronic supplementary information (ESI) available. See DOI: 10.1039/c7cp06085h

photocatalytic systems could lead to an enhanced photocatalytic activity under visible light irradiation.

Considering the material development aspects, the construction of photocatalysts based on hollow/spongy like spherical nanostructures is believed to be an effective strategy to improve their photocatalytic activities.[11] A hollow/spongy like spherical structure that was constructed using solid nanoparticles can improve the photo-induced charge separation and promote the charge carriers to the surrounding molecules by lowering their travel path to the surface of the particles.[12] Also, such structures inherently possess porous-like structures that greatly enhance the accessibility of active sites by the reactant molecules. In addition, multiple scattering of light within their interiors allows the absorption of light more efficiently.[13,14] It should be noted that compared to the number of studies carried out on the development of metal oxide based nanostructures,[15] there are only limited studies that have been carried out on metal sulfide-based nanostructures. This is essentially due to the complexities involved in synthesizing metal sulfide materials at a nanoscale. For instance, Lou *et al.*[16] have successfully fabricated multi-shelled $NiCo_2S_4$ by using the anion exchange method and they found that the $NiCo_2S_4$ hollow spheres exhibited uniform morphology with much higher conductivity in comparison with their metal oxides.

In this context, this study is the first to report the synthesis of highly uniform spongy-like spheres of $CdIn_2S_4$ through an alcoholysis mediated sulfidation process. This fabrication process is essentially a one-pot synthesis of CdIn@glycerate solid spheres followed by calcination and sulfidation to achieve spongy-like spheres of $CdIn_2S_4$ phase. Furthermore, Ni was deposited as a co-catalyst onto $CdIn_2S_4$ and the photocatalytic hydrogen production efficiency under solar light irradiation was investigated, and compared with the efficiency of noble metals such as Pt and Pd deposited on $CdIn_2S_4$ spongy-like spheres.

2. Experimental

2.1 Chemicals

Glycerol, indium(III) nitrate hexahydrate, cadmium(II) nitrate hexahydrate, ammonium nickel(II) sulfate hexahydrate, isopropanol, and ethanol were purchased from a commercial source, Alfa Aesar. All reagents were directly used without further purification.

2.2 Material syntheses

The synthesis of mixed cadmium–indium metal sulfides (denoted as CIS-x; where x represents the In/Cd molar ratio (where x is 3.0, 2.0, 1.0 and 0.5)). The synthesis process consisted of three steps: (i) synthesis of CdIn@glycerate templates: in a typical synthesis, different ratios of In/Cd precursors and 8 mL of glycerol were dissolved completely in 40 mL of isopropanol to form a colorless solution. Then, the solution was transferred into a Teflon-lined stainless steel autoclave and kept at 180 °C for 6 h. After cooling to room temperature naturally, the brown white precipitate was separated by centrifugation, washed several times with anhydrous ethanol and dried in an oven at 80 °C to obtain CdIn@glycerate templates. (ii) Synthesis of $CdIn_2O_4$ spongy-like spheres: in order to obtain the $CdIn_2O_4$ spongy-like spheres (denoted as CIO-x), the as-synthesized CdIn@glycerate solid spheres were then calcined at 500 °C in air for 3 h with a slow heating rate of 1 °C per min. (iii) Preparation of $CdIn_2S_4$ spongy-like spheres: 100 mg of the obtained $CdIn_2O_4$ was treated under a H_2S atmosphere at 450 °C for 3 h.

2.3 Characterization

The transmission electron microscopy (TEM) images of the samples were obtained using a JOEL JEM 1230 operated at 120 kV, and high-resolution TEM (HRTEM) images were obtained using a Philips G2 F30 Tecnai instrument operated at 300 kV. The scanning electron microscopy (SEM) images were obtained using a JEOL 6360 operated at 15 kV. Powder X-ray diffraction (XRD) patterns of the samples were obtained using a Bruker SMART APEXII X-ray diffractometer equipped with a Cu Kα radiation source (λ = 1.5418 Å). X-ray photoelectron spectroscopy (XPS) measurements were carried out in the ion-pumped chamber (evacuated to 10^{-9} Torr) of a photoelectron spectrometer (Kratos Axis-Ultra) equipped with a focused X-ray source (Al Kα, $h\nu$ = 1486.6 eV). UV-Vis spectra were recorded on a Cary 300 Bio UV-visible spectrophotometer. N_2 adsorption–desorption isotherms of the samples were obtained at 77 K using a Quantachrome Autosorb-1 MP analyzer. Prior to the respective measurements, the samples were out-gassed under vacuum for 6 h at 150 °C.

2.4 Photocatalytic activity test

All the photocatalytic reactions were conducted in a home-built top-irradiated reactor at an ambient temperature and atmospheric pressure. Initially, 100 mg of photocatalyst was dispersed for the photo-deposition of Ni, Pt and Pd separately (at an optimum amount of 3 wt%) prior to the photocatalytic tests. In a typical photocatalytic experiment, an optimized amount of 5 mg of the co-catalyst loaded photocatalyst was dispersed in a solution containing 9 mL of water and 1 mL of sacrificial agent (Triethanolamine/TEOA) and taken in the reactor cell. After that, the mixture was purged with nitrogen for 10 min. Then, the reactor cell was illuminated using a solar simulator at 100 W for 3 h. For the recyclability test, the reactor cell was purged again with nitrogen for 30 min, before the start of each cycle. The recycling studies were conducted for 9 h in 3 cycles and each cycle was carried out for 3 h. The amount of H_2 gas generated was determined using a gas chromatograph equipped with a thermal conductivity detector (TCD), and using N_2 as the carrier gas.

3. Results and discussion

The formation mechanism of the $CdIn_2S_4$ (CIS) spongy-like spheres is schematically illustrated in Fig. 1. As described above, firstly the CdIn@glycerate templates were prepared based on the general alcoholysis mechanism.[17] Then, the

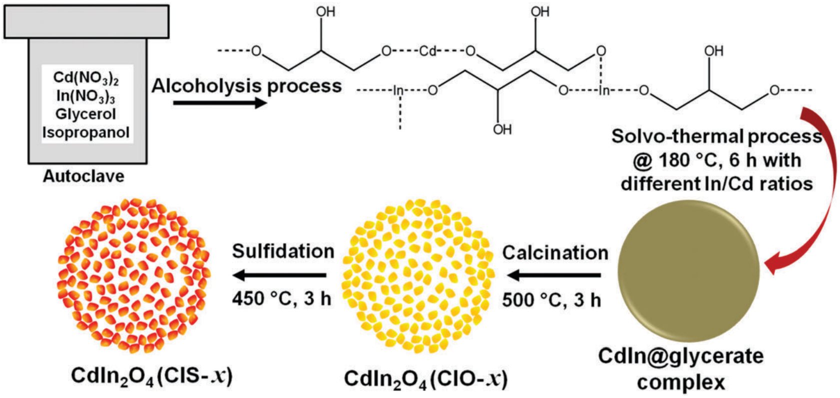

Fig. 1 Formation mechanism of the CIO-*x* and CIS-*x* spongy-like spheres.

Cd^{2+} and In^{3+} precursors were diluted with glycerol ligand to form a bimetallic CdIn–glycerol complex. At high temperature and pressure, glycerol was polymerized into esters along with the elimination of water, where the water initiated the hydrolysis process of CdIn–glycerol complexes and led to the production of CdIn@glycerate templates. Then, the process of calcination under air removed the glycerate core, leading to the formation of $CdIn_2O_4$ (CIO-*x*) spheres. In the next step, CIO-*x* was transformed to CIS-*x* by a sulfidation process under H_2S treatment as shown in Fig. 1. After H_2S treatment, the color of the prepared sample changed from pale-yellow to bright-yellow. The formation of CIS-*x* can be attributed to the anion exchange reaction in the CIO-*x*. The inward diffusion of H_2S gas in CIO-*x* spheres leads to the inclusion of S in the lattices of CIO-*x*, which replaces the oxygen with sulfur species at higher temperatures and leads to the formation of CIS-*x* compositions. Then, these synthesized CIS-*x* compositions were further deposited with Ni at an optimized concentration of 3 wt%. The photo-deposition of Ni onto the CIS-2.0 sample was confirmed through the observed color changes from bright-yellow to grayish-yellow as shown in Fig. S1 (ESI†).

The influence of off-stoichiometric In/Cd ratios on the structural and optical absorption characteristics of the $CdIn_2S_4$ phase was studied using X-ray diffraction and UV-visible absorption spectroscopy and the obtained results are shown in Fig. 2(A) and (B), respectively. The XRD patterns reveal the spinel structure with enhanced crystalline properties of the CIS-*x* samples as shown in Fig. 2(A). The peaks at $2\theta = 27^\circ$ and 43.5° corresponding to (311) and (440) are the two characteristic diffraction planes of single phase $CdIn_2S_4$ (JCPDS card #027-0060).[18,19] The observed small peaks corresponding to the (002) plane for the samples CIS-1.0 and CIS-0.5 (lines c and d in Fig. 2(A)) indicate the presence of a hexagonal CdS phase. The formation of a CdS phase could be possible because of the precipitation of excess Cd^{2+} ions owing to their poor solubility product constant.[5] This essentially shows the evolution process of the $CdIn_2S_4$ phase with respect to the tunable In/Cd ratios.

The UV-Vis absorption spectra of the synthesized CIS-*x* samples are given in Fig. 2(B). It can be seen that the CIS-*x* samples show noticeable visible light absorption band edges. This indicates that these materials can exhibit strong optical activities under visible light. It is noteworthy that the decreasing In/Cd ratio tends to influence the visible light activity of the materials as slight changes can be observed in the region from 350 nm to 500 nm.

Fig. 3 shows the amount of hydrogen generated over Ni-CIS-*x* compositions with different In/Cd ratios. Among the samples,

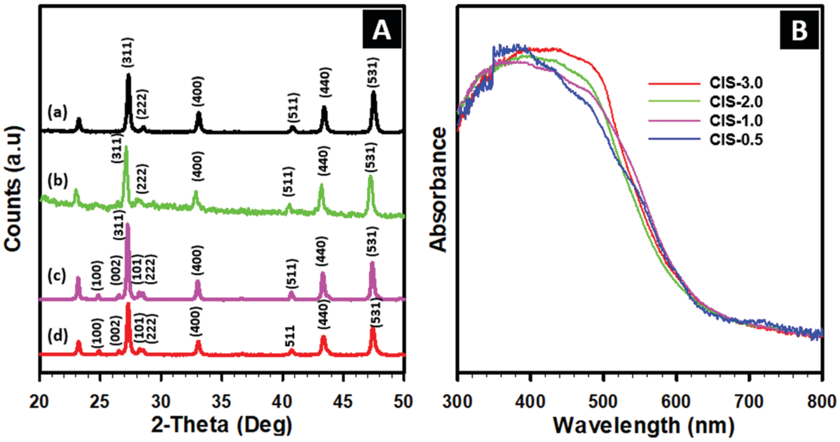

Fig. 2 (A) XRD pattern and (B) UV-Vis spectra of $CdIn_2S_4$ with different precursor ratios: (a) 3.0, (b) 2.0, (c) 1.0 and (d) 0.5.

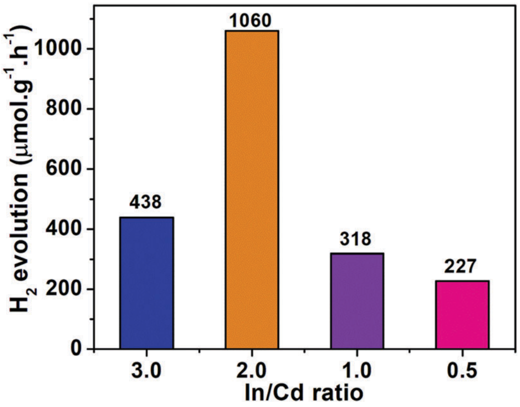

Fig. 3 Photocatalytic hydrogen evolution over Ni deposited CIS-*x* photocatalysts (where *x* = 3.0, 2.0, 1.0 and 0.5).

Ni-CIS-2.0 showed the highest photocatalytic hydrogen evolution of 1060 μmol g^{-1} h^{-1}. It is observed that an increasing concentration of In^{3+} or Cd^{2+} leads to a significant decrement in the H_2 evolution. As shown in Fig. 3, the average amount of hydrogen produced was calculated to be 227, 318 and 448 μmol g^{-1} h^{-1} for Ni-CIS-0.5, Ni-CIS-1.0, and Ni-CIS-3.0, respectively. It is expected that when the In/Cd ratio is lower than 2.0, it leads to off-stoichiometry in the $CdIn_2S_4$ phase, resulting in the formation of In_2S_3 and CdS phases due to the existence of excess Cd^{2+} or In^{3+} ions in the CIS-*x* compositions. Thereby, the presence of In_2S_3 or CdS, as impurity phases, considerably limits the photocatalytic activity as these impurities affect the charge separation and band edge position of the host $CdIn_2S_4$ phase.[5]

Among the Ni-CIS-*x* samples, Ni-CIS-2.0 showed enhanced photocatalytic hydrogen evolution and therefore this sample was taken for further extensive analysis to understand the photocatalytic mechanism. In addition, the photocatalytic performance of the Pt and Pd deposited CIS-2.0 samples was also studied in terms of their photocatalytic hydrogen evolution efficiencies under sunlight in comparison with the Ni deposited CIS-2.0 sample.

Fig. 4(A)–(C) show SEM images of the CdIn@glycerate templates, CIO-2.0 ($CdIn_2O_4$), and CIS-2.0 ($CdIn_2S_4$) spongy-like spheres, respectively. The size of the CdIn@glycerate template spheres is quite uniform with a diameter in the range of 600–700 nm, which is found to be decreased to 400–500 nm after calcination at 500 °C and transformed to the spongy-like structure due to the complete combustion of the glycerate core. The existence of spongy-like morphology can be seen in Fig. 4(B) and (C), where the broken spheres show clearly the hollowness inside the spheres as shown in the inset image of Fig. 4(B) and (C).

It was observed that after the sulfidation process at 450 °C for 3 h, the color of the sample changed from pale-yellow to bright-yellow, suggesting the formation of the sulfide phase of the material. Furthermore, the observed spongy-like morphology of the materials was also confirmed from the obtained TEM images as shown in Fig. 4(D) and (E), respectively. It is noteworthy that the surface of the spongy-like spheres has become rough after the sulfidation process. Interestingly, Fig. 4(F) shows the TEM image of the broken CIS-2.0 spheres that essentially reveals that these spongy-like spheres are composed of numerous closely packed nanoparticles of the average size of 25 nm, which is obtained through alcoholysis followed by the sulfidation process. The average crystallite size of CIS-2.0 was also calculated using Scherrer's formula ($d = 0.9\lambda/\beta\cos\theta$, where *d*-crystallite size, 0.9-shape factor, λ-wavelength of the incident X-rays, β-full width at half maximum and $\cos\theta$-diffraction angle) corresponding to the (311) and (440) plane and it was found to

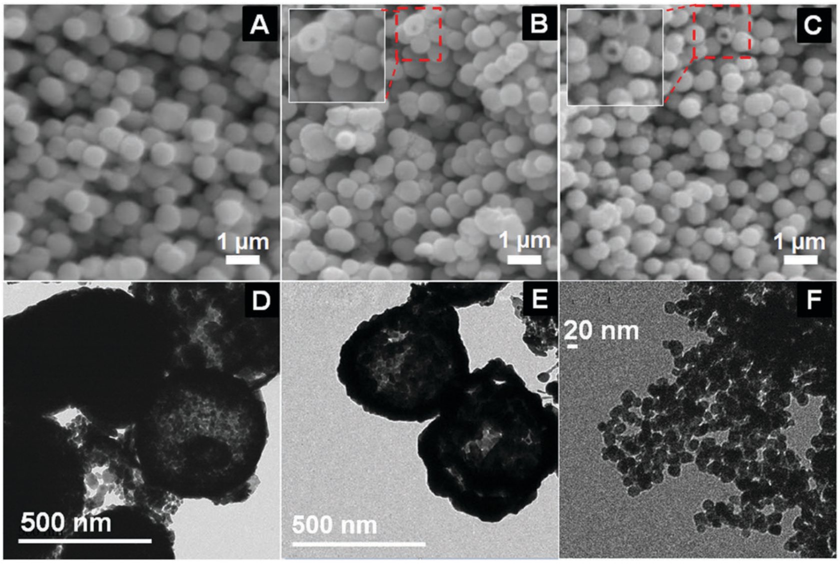

Fig. 4 (A–C) The SEM images of CdIn@glycerate template spheres, and CIO-2.0 and CIS-2.0 spongy-like spheres, respectively, and (D) and (E) the respective TEM images of the spongy-like spheres and (F) CIS-2.0 spheres broken into smaller nanoparticles. (The inset image shows a closer view of the respective morphology.)

be 22 nm, and this observation was also found to be consistent with the respective TEM image of the sample (Fig. 4(F)). The energy dispersive X-ray spectroscopy (EDS) analysis of the CIO-2.0 sample confirmed the presence of the elements Cd, In and O (given in the ESI,† Fig. S2). Similarly, the EDS spectrum of the CIS-2.0 samples, as shown in the ESI,† Fig. S3, confirmed the existence of Cd, In, and S in the material. It should be noted that oxygen is not observed in the CIS-2.0 sample, suggesting the complete sulfidation of the material. Furthermore, the peak corresponding to Au appeared in the spectra because of the sputtering of Au onto the samples during their electron microscopy imaging analysis.

For comparison, Fig. 5(A) shows the XRD pattern of the CIO-2.0 sample. The diffraction peaks at 2θ = 27°, 32° and 34° indexed to (220), (311) and (222) are the characteristic planes of spinel structured $CdIn_2O_4$ phase. These peaks with high intensity indicate the enhanced crystalline properties of the sample. However, the diffraction peaks at 30.5° and 35° corresponding to (222) and (400) planes and 33° and 39° corresponding to (111) and (200) planes indicate the existence of In_2O_3 and CdO phases, respectively, in the sample. The co-existence of In_2O_3 and CdO impurity phases could originate from the presence of point defects such as oxygen vacancies or the interchange of Cd^{2+} and In^{3+} ions that could be due to the insufficient reaction conditions.[20] On the other hand, the XRD pattern of the sulfide-sample ($CdIn_2S_4$) indicates the formation of a single phase of the material, where it essentially suggests that the H_2S treatment induces the complete replacement of O ions as well as oxygen vacancies by S ions.

The UV-Vis absorption spectra of the CIO-2.0 and CIS-2.0 samples are shown in Fig. 5(B). The observed prominent red shift in the absorption edge of CIS-2.0 could be originated due to the transformation of the oxide phase into the sulfide phase. The observed hump like peak in the UV region (around 320 nm) may be due to the presence of impurity phases in the CIO-2.0 sample, while the smooth absorption edge indicates the single phase nature of the CIS-2.0 sample, which is in good agreement with the obtained XRD result. It should be noted that the absorption range of the CIO-2.0 sample was observed up to 640 nm, while it was extended up to 780 nm for the CIS-2.0 sample. This observed enhancement is much higher than those reported in the literature.[21–26] The inset image in Fig. 5(B) shows the $(\alpha h\nu)^{1/2}$ *versus* photon energy curve that is plotted using the Kubelka–Munk function for the estimation of the band gap energy of the samples. Accordingly, the estimated band gap of CIS-2.0 and CIO-2.0 was found to be 2.23 and 2.61 eV, respectively. It is known that the band edge potential of the conduction band (E_{CB}) and valence band (E_{VB}) is an important parameter to validate the suitability of materials for photocatalytic applications. For an efficient water splitting reaction, the band edge position of the conduction band should be located above the hydrogen evolution potential, while the valence band edge potential should be below the O_2/H_2O potential.[1] Accordingly, the E_{VB} and E_{CB} potential of the CIS-2.0 sample was calculated using the empirical formula,[21,24] $E_{CB} = X - E^{e} - 0.5E_g$ and $E_{VB} = E_{CB} + E_g$ (detailed calculations can be found in the ESI†) where X is the absolute electronegativity of the semiconductor ($CdIn_2S_4$), and E^{e} is the difference between the normal hydrogen electrode (NHE) and the vacuum that has a value of ∼4.5 eV. Based on the equations, the bottom of the conduction band and the top of the valence band of CIS-2.0 is determined to be −0.73 eV and +1.50 eV, respectively. From the obtained values, the conduction band edge potential is found to be more negative than the H^+/H_2 (E = 0 eV) potential and the valence band edge is more positive than the O_2/H_2O potential (E = +1.23 eV), indicating that $CdIn_2S_4$ could be an efficient visible light driven photocatalyst for water splitting, particularly for hydrogen generation.

The specific surface area of the sample was measured by N_2 adsorption–desorption isotherms analysis and the obtained curves are shown in Fig. S4 (ESI†). It is found that the CIO-2.0 possesses a specific surface area of 26 $m^2\ g^{-1}$, which is found to be decreased to 19 $m^2\ g^{-1}$ for CIS-2.0. This could be attributed to the replacement of oxygen ions by sulfur ions in the material that increased the molecular weight of the CIS-2.0 composition and decreased the surface area.

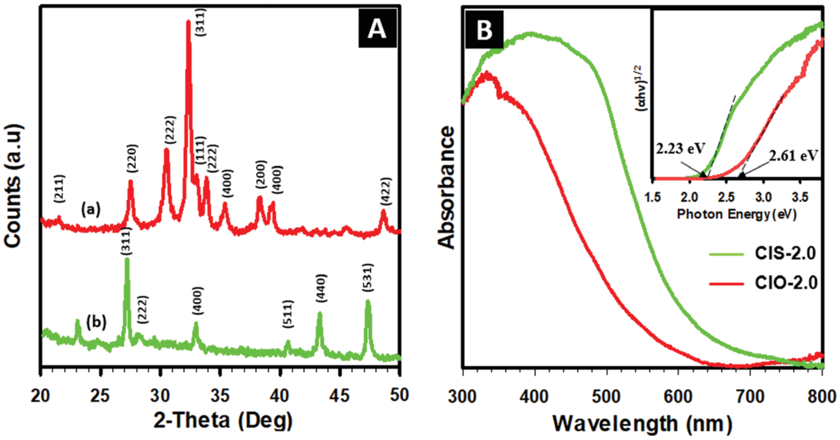

Fig. 5 (A) XRD spectra of (a) CIO-2.0 and (b) CIS-2.0; (B) UV-Vis spectra of CIO-2.0 and CIS-2.0; inset image: estimation of the band gap energy of CIS-2.0 and CIO-2.0.

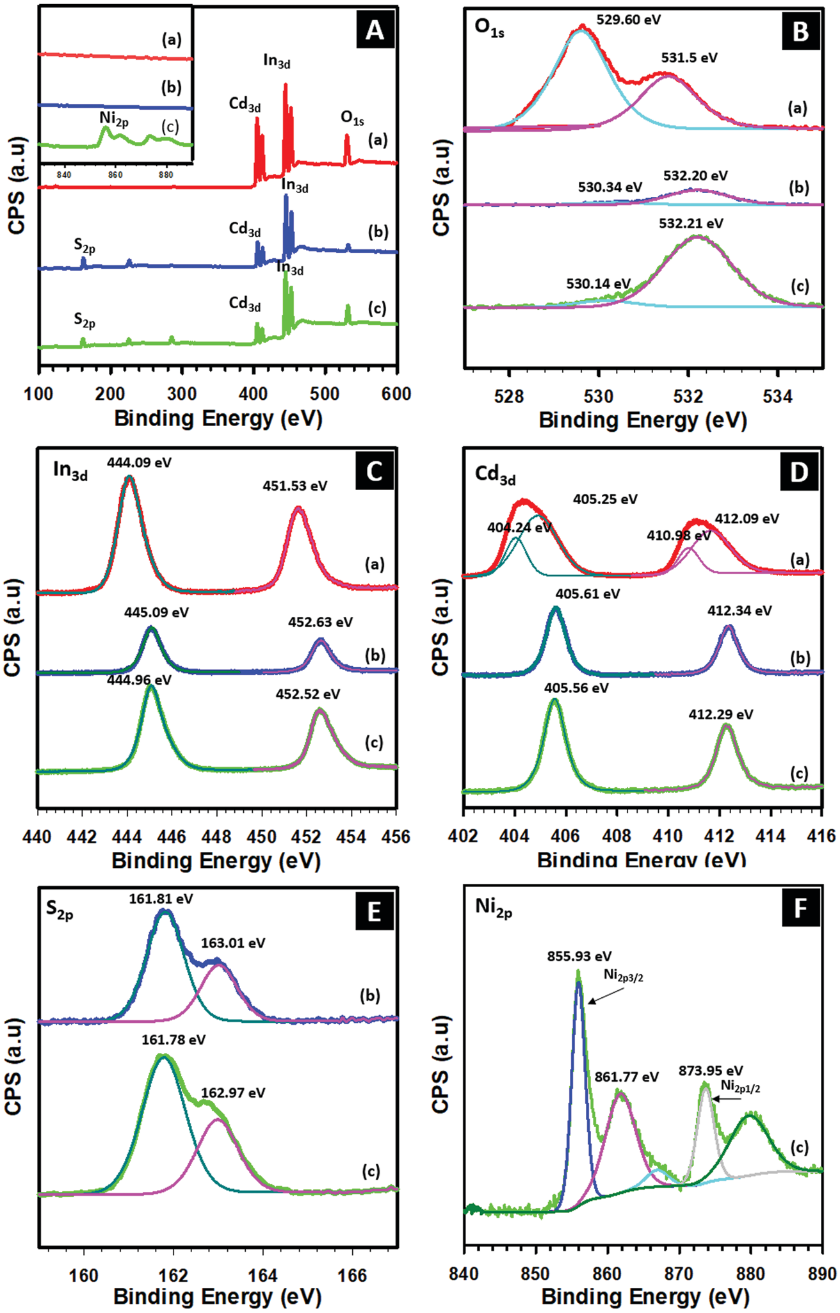

Fig. 6 XPS (A) survey spectra, (B) O 1s, (C) In 3d, (D) Cd 3d, (E) S 2p, and (F) Ni 2p; Inset: (a) CIO-2.0, (b) CIS-2.0 and (c) Ni-CIS-2.0.

The surface chemical state of CIO-2.0, CIS-2.0, and Ni-CIS-2.0 was examined using the XPS technique. The survey XPS spectra as shown in Fig. 6(A) indicate the existence of Cd, In, O, S and Ni in their respective samples. The corresponding high-resolution XPS spectra of O 1s, In 3d, Cd 3d, S 2p and Ni 2p of all three samples are given in Fig. 6(B)–(F). As seen in the O 1s spectrum of CIO-2.0 (Fig. 6(B)), the de-convoluted peak centered at 529.6 eV can be assigned to the metal-oxide bond and the peak appearing at 531.5 eV may have originated from the surface adsorbed H_2O and CO_2 under the high-temperature air pyrolysis. On the other hand, the only peak that appeared at around 532.2 eV for the CIS-2.0 and Ni-CIS-2.0 samples could be attributed to the adsorbed oxygen on their surface. The disappearance of the peak at lower binding energies corresponding to the lattice oxygen suggested a complete sulfidation of CIO-2.0 into CIS-2.0. The XPS spectra of In 3d can be fitted to two separated peaks as shown in Fig. 6(C). For the CIO-2.0, the two peaks at 444.0 and 451.5 eV can be attributed to In $3d_{5/2}$ and In $3d_{3/2}$, respectively.[27] After sulfidation (CIS-2.0), these peaks have been found to be shifted by ~1.0 eV towards higher binding energy and centered at 445.0 and 452.6 eV. This could be attributed to the transformation of an indium–oxide bond into indium–sulfide form. Moreover, the replacement of larger electronegativity elements (oxygen) with smaller electronegativity elements (sulfur) might have increased the electron density of the In^{3+} cation and thereby these peaks are slightly shifted towards higher binding energy for CIS-2.0 over CIO-2.0.

Fig. 6(D) shows the high-resolution Cd 3d XPS spectrum of CIO-2.0 (line a), CIS-2.0 (line b) and Ni/CIS-2.0 (line c). The strong peaks of CIO-2.0 centered at 405.2 and 412.0 eV revealed the peaks corresponding to Cd $3d_{5/2}$ and Cd $3d_{3/2}$, respectively, which indicated the existence of Cd ions with a +2 oxidation state as observed in spinel structures.[28] Similarly, the other two weak peaks with binding energies of 404.24 and 410.9 eV were also deconvoluted in the Cd 3d XPS spectrum of CIO-2.0. These peaks can be ascribed to the Cd $3d_{5/2}$ and Cd $3d_{3/2}$ lines corresponding to the +2 oxidation state of Cd ions as in cadmium oxides. These results are in good agreement with their corresponding XRD results that confirmed the presence of the cadmium oxide impurity phase in the $CdIn_2O_4$ spinel structure. Interestingly, only two peaks at 405.6 and 412.3 eV were observed in the Cd 3d XPS specrtum for the CIS-2.0 and Ni-CIS-2.0 samples, which can be assigned to Cd $3d_{5/2}$ and Cd $3d_{3/2}$ lines indicating the Cd^{2+} oxidation state in the spinel phase. The disappearance of two peaks at 404.24 and 410.9 eV can be interpreted by the complete sulfidation of mixed oxides (CdO, In_2O_3, and $CdIn_2O_4$) to form a single phase of spinel structure ($CdIn_2S_4$) under H_2S gas treatment at high temperature. The S 2p spectra of CIS-2.0 and Ni/CIS-2.0 are shown in Fig. 6(E). These signals can be divided into two separate peaks at 161.11 and 162.31 eV, corresponding to the binding energy of S $2p_{3//2}$ and S $2p_{1/2}$ lines indicating the −2 oxidation of S in $CdIn_2S_4$.[29] From the obtained XPS results, it was found that all the elements present in the CIO-2.0, CIS-2.0, and Ni-CIS-2.0 possess their respective native-stable oxidation states that eventually indicate the appropriate chemical composition and structural integrity of the obtained materials.

As described above, metallic Ni as a co-catalyst was deposited on the surface of CIS-2.0 spongy-like spheres through chemical photo-reduction of a nickel precursor and its mechanism can be described as follows. Under light irradiation, electrons will be excited form the VB (+1.50 eV *vs.* NHE) to the CB (−0.73 eV *vs.* NHE) and these excited electrons reduce Ni^{2+} species into metallic Ni particles as the Ni^{2+}/Ni potential (−0.257 eV *vs.* NHE) is much lower than the CB level of $CdIn_2S_4$ and this led to the deposition of Ni onto the surface of CIS. However, the XPS spectra of Ni $2p_{3/2}$ and Ni $2p_{1/2}$ of the Ni-CIS-2.0 sample show two peaks at a binding energy of 855.93 and 873.95 eV, which is the characteristic peaks of NiO[30] and also the peak corresponding to Ni $2p_{3/2}$ at 861.77 eV indicates the Ni^{2+} in Ni species.[31] The absence of a firm peak corresponding to metallic Ni could be due to the existence of adsorbed oxygen species on the surface of the $CdIn_2S_4$ sample, which could be due to the exposure of the sample to the air.[32]

The photocatalytic hydrogen evolution efficiency of the CIS-2.0 sample with different co-catalyst loading such as Ni, Pt, and Pd is displayed in Fig. 7(A). The photocatalytic hydrogen generation of Ni-CIS-2.0 was found to be much higher than that of Pt-CIS-2.0 and Pd-CIS-2.0 samples. From the obtained results, the amount of H_2 production was estimated to be 1060 μmol g^{-1} h^{-1}, which is much higher than the H_2 produced by Pt-CIS-2.0 (180 μmol g^{-1} h^{-1}) and Pd-CIS-2.0 (290 μmol g^{-1} h^{-1}) samples. In addition to this, the recyclability of the Ni-CIS-2.0 photocatalyst was also evaluated and it showed an enhanced stability over 3 cycles (for 9 h) without any significant decrement in its activity (Fig. 7(B)). This suggests that Ni-CIS-2.0 could be a promising photocatalyst for hydrogen evolution and water splitting applications.

Based on the above experimental results, the possible mechanism for the hydrogen generation efficiency of Ni-CIS-2.0 spongy-like spheres is proposed and depicted in Fig. 8. Under light irradiation, the electrons are excited from the valence band (VB) to the conduction band (CB) of CIS and the excited electrons are further transferred to the nickel that is deposited on the surface of the photocatalyst. Consequently, water molecules are reduced into hydrogen by the photo-induced electrons on the metallic nickel. Meanwhile, the holes in the VB of $CdIn_2S_4$ are consumed by the sacrificial agent TEOA.

As mentioned, at a given amount of metal (Ni, Pt, Pd) loading, Ni-CIS showed the highest photocatalytic activity, followed by Pd and Pt, respectively. In order to validate these observations, the physical and electrochemical properties of all

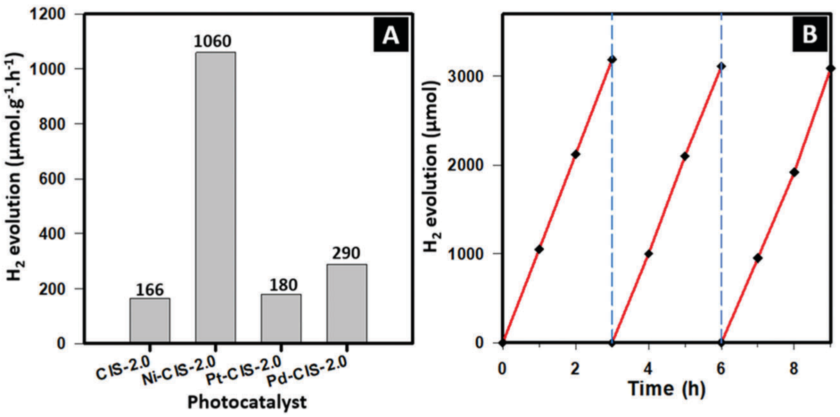

Fig. 7 (A) Sunlight driven photocatalytic hydrogen production efficiency of CIS-2.0 spongy-like spheres with different co-catalyst loading and (B) recyclable efficiency of Ni-CIS-2.0.

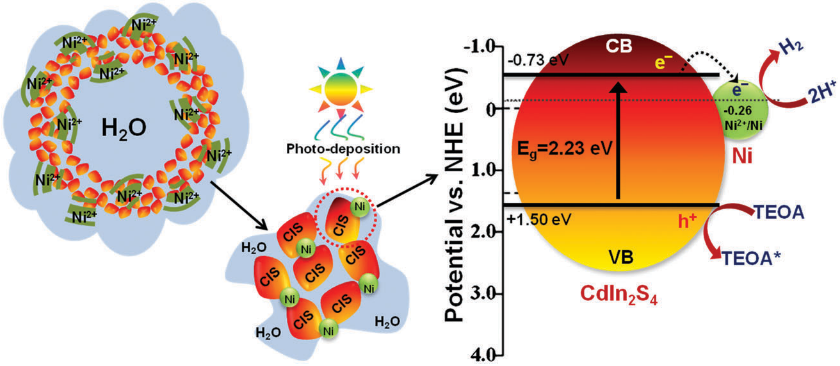

Fig. 8 Illustration of the formation and photocatalytic hydrogen evolution mechanism of the Ni-CIS-2.0 photocatalyst under solar light.

Table 1 Electro-chemical properties of the co-catalyst employed.[33]

Element	Electronegativity (pauling scale)	Electron affinity (eV)	Work function (eV)
Ni	1.91	1.16	5.04–5.35
Pt	2.28	0.56	5.22–5.60
Pd	2.20	2.13	5.12–5.93

three metals should be considered[26] and the relevant properties are given in Table 1.

Firstly, the electronegativity of all three metal co-catalysts (Ni, Pt, Pd) as compared to that of the host (Cd, In): as given in Table 1, the electronegativity of Ni is likely in the range of Cd (1.69 eV) and In (1.78 eV), while that of Pt and Pd is relatively very high. The equivalence in the electronegativity of these elements constitutes the favorable reaction sites for the effective transportation of electrons from the CB of $CdIn_2S_4$ to the Ni. It should be noted that the CB of $CdIn_2S_4$ is composed of Cd and In species, and the VB is composed of S species.[34] Accordingly, the increased electronegativity of the noble metal co-catalysts Pt and Pd causes mismatch of electron transfer potential between the host and co-catalysts that significantly affects the photocatalytic activities of Pt and Pd supported $CdIn_2S_4$ photocatalysts.[35] Secondly, the electron affinity of the metal co-catalysts: fundamentally, the electron affinity of the supported co-catalyst should be adequate enough to sustain the stability of photo-induced electrons until the proton reduction reaction occurs on the photocatalyst surface. Accordingly, any metals with high or low electron affinity may unfavorably limit the release of trapped electrons to the water molecules. This probably leads to the lower photocatalytic effect in the Pt and Pd supported $CdIn_2S_4$ as compared to the Ni supported $CdIn_2S_4$ photocatalyst.[36] Thirdly, the work function of the co-catalysts: as given in Table 1, the work function of Ni is relatively lower as compared to Pt and Pd with respect to the CB potential of the host photocatalyst $CdIn_2S_4$. Thereby, the Ni co-catalyst possibly enhances the hydrogen production by effective transfer of electrons to the surrounding water molecules more efficiently than that of the Pt and Pd co-catalysts. Therefore, the Ni-$CdIn_2S_4$ photocatalyst showed enhanced photocatalytic hydrogen production properties as compared to the Pt and Pd supported $CdIn_2S_4$.

4. Conclusion

In summary, nickel supported $CdIn_2S_4$ (Ni-CIS) spongy-like spheres were successfully prepared through a novel one-pot solvothermal alcoholysis mediated sulfidation process. The obtained hydrogen production efficiency of Ni-CIS was found to be around 6.3, 5.5 and 3.6 fold higher than that of the bare, Pt and Pd supported $CdIn_2S_4$, respectively. The observed enhanced photocatalytic activity of Ni-CIS was attributed to a strong visible light absorption and the synergistic interaction between the host CIS photocatalyst and nickel co-catalyst. From the obtained results, $CdIn_2S_4$ that was supported with Ni as a co-catalyst could be realized as a more promising photocatalyst, over noble-metal supported photocatalysts, towards hydrogen production under sunlight irradiation.

Conflicts of interest

There are no conflicts to declare.

Acknowledgements

This work was supported by the Natural Science and Engineering Research Council of Canada (NSERC) through the Collaborative Research and Development (CRD), Strategic Project (SP) and Discovery Grants. The author would like to thank EXP Inc. and SiliCycle Inc. for their support.

References

1 K. Zhang and L. Guo, *Catal. Sci. Technol.*, 2013, **3**, 1672–1690.
2 Z. Yue, A. Liu, C. Zhang, J. Huang, M. Zhu, Y. Du and P. Yang, *Appl. Catal., B*, 2017, **201**, 202–210.
3 Y. Wu, Z. Yue, A. Liu, P. Yang and M. Zhu, *ACS Sustainable Chem. Eng.*, 2016, **4**, 2569–2577.
4 Y. Shiga, N. Umezawa, N. Srinivasan, S. Koyasu, E. Sakai and M. Miyauchi, *Chem. Commun.*, 2016, **52**, 7470–7473.
5 A. Bhirud, N. Chaudhari, L. Nikam, R. Sonawane, K. Patil, J.-O. Baeg and B. Kale, *Int. J. Hydrogen Energy*, 2011, **36**, 11628–11639.

6 J.-P. Song, P.-F. Yin, J. Mao, S.-Z. Qiao and X.-W. Du, *Nanoscale*, 2017, **9**, 6296–6301.

7 X. Pan, M.-Q. Yang, X. Fu, N. Zhang and Y.-J. Xu, *Nanoscale*, 2013, **5**, 3601–3614.

8 M. Zhu, X. Cai, M. Fujitsuka, J. Zhang and T. Majima, *Angew. Chem., Int. Ed.*, 2017, **56**, 2064–2068.

9 X. Yue, S. Yi, R. Wang, Z. Zhang and S. Qiu, *Sci. Rep.*, 2016, **6**, 22268.

10 Y. Wang, J. Wu, J. Zheng, R. Jiang and R. Xu, *Catal. Sci. Technol.*, 2012, **2**, 581–588.

11 C. C. Nguyen, N. N. Vu and T.-O. Do, *J. Mater. Chem. A*, 2015, **3**, 18345–18359.

12 J. B. Joo, Q. Zhang, I. Lee, M. Dahl, F. Zaera and Y. Yin, *Adv. Funct. Mater.*, 2012, **22**, 166–174.

13 Z. Wang, J. Hou, C. Yang, S. Jiao, K. Huang and H. Zhu, *Energy Environ. Sci.*, 2013, **6**, 2134–2144.

14 H. Li, Z. Bian, J. Zhu, D. Zhang, G. Li, Y. Huo, H. Li and Y. Lu, *J. Am. Chem. Soc.*, 2007, **129**, 8406–8407.

15 C.-C. Nguyen, N.-N. Vu and T.-O. Do, *J. Mater. Chem. A*, 2016, **4**, 4413–4419.

16 L. Shen, L. Yu, H. B. Wu, X.-Y. Yu, X. Zhang and X. W. Lou, *Nat. Commun.*, 2015, **6**, 6694.

17 A. Vioux, *Chem. Mater.*, 1997, **9**, 2292–2299.

18 S. K. Batabyal, S. E. Lu and J. J. Vittal, *Cryst. Growth Des.*, 2016, **16**, 2231–2238.

19 C. Ling, X. Ye, J. Zhang, J. Zhang, S. Zhang, S. Meng, X. Fu and S. Chen, *Sci. Rep.*, 2017, **7**, 27.

20 F. F. Yang, L. Fang, S. F. Zhang, J. S. Sun, Q. T. Xu, S. Y. Wu, J. X. Dong and C. Y. Kong, *Appl. Surf. Sci.*, 2008, **254**, 5481–5486.

21 M. V. Carevic, M. I. Comor, M. N. Mitric, T. S. Barudzija, S. P. Ahrenkiel and N. D. Abazovic, *CrystEngComm*, 2015, **17**, 8492–8499.

22 X. Chen, L. Li, W. Zhang, Y. Li, Q. Song and L. Dong, *ACS Sustainable Chem. Eng.*, 2016, **4**, 6680–6688.

23 D. Li, F. Shi, D. Jiang, M. Chen and W. Shi, *RSC Adv.*, 2017, **7**, 231–237.

24 S. Li, Y.-H. Lin, B.-P. Zhang, J.-F. Li and C.-W. Nan, *J. Appl. Phys.*, 2009, **105**, 054310.

25 A. Habibi-Yangjeh and M. Shekofteh-Gohari, *Sep. Purif. Technol.*, 2017, **184**, 334–346.

26 Y. Yu, G. Chen, G. Wang and Z. Lv, *Int. J. Hydrogen Energy*, 2013, **38**, 1278–1285.

27 H. I. Yeom, J. B. Ko, G. Mun and S. H. K. Park, *J. Mater. Chem. C*, 2016, **4**, 6873–6880.

28 R. J. Deokate, *Superlattices Microstruct.*, 2014, **76**, 16–25.

29 M. N. Ghazzal, R. Wojcieszak, G. Raj and E. M. Gaigneaux, *Beilstein J. Nanotechnol.*, 2014, **5**, 68–76.

30 C.-T. Dinh, M.-H. Pham, F. Kleitz and T.-O. Do, *J. Mater. Chem. A*, 2013, **1**, 13308–13313.

31 X. Zou, J. Su, R. Silva, A. Goswami, B. R. Sathe and T. Asefa, *Chem. Commun.*, 2013, **49**, 7522–7524.

32 A. K. Agegnehu, C.-J. Pan, J. Rick, J.-F. Lee, W.-N. Su and B.-J. Hwang, *J. Mater. Chem.*, 2012, **22**, 13849–13854.

33 L. Pauling, *Nature of the Chemical Bond*, Cornell University Press, New York, 1960.

34 A. Kudo and Y. Miseki, *Chem. Soc. Rev.*, 2009, **38**, 253–278.

35 S. Onsuratoom, T. Puangpetch and S. Chavadej, *Chem. Eng. J.*, 2011, **173**, 667–675.

36 P. D. Tran, L. Xi, S. K. Batabyal, L. H. Wong, J. Barber and J. S. Chye Loo, *Phys. Chem. Chem. Phys.*, 2012, **14**, 11596–11599.